Comparison of the microstructure, mechanical properties and distortion of stainless steel 316L fabricated by micro and conventional laser powder bed fusion

Jin Fu[a], Shuo Qu[b], Junhao Ding[b], Xu Song [b,*], M.W. Fu[a,**]

[a] Department of Mechanical Engineering, The Hong Kong Polytechnic University, Hung Hom, Kowloon, Hong Kong, China

[b] Department of Mechanical and Automation Engineering, Chinese University of Hong Kong, Shatin, Hong Kong, China

[*] Corresponding author.
[**] Corresponding author.
Email address: xsong@cuhk.edu.hk (Xu Song), mmmwfu@polyu.edu.hk (M.W. Fu).

Abstract

Micro laser powder bed fusion (μLPBF) technology offers great benefits to industries as it enables fabrication of complicated metallic components with greater accuracy and minimum feature size as small as 50 μm. Employing finer laser beam and smaller metal powder in μLPBF leads to many variations from the conventional LPBF (cLPBF) in terms of microstructure, mechanical properties and distortion, which have not yet been well understood. This work provides a comparative study of the μLPBF and cLPBF of the well-known material, stainless steel 316L based on the surface quality, crystal structure, solidification microstructure, tensile properties and distortion of as-printed parts, and their sensitivities to μLPBF process parameters are also studied. Results show that lower surface roughness (Ra=3.4 μm for top surfaces) is obtained after μLPBF. Stronger <110> texture along building direction is developed in the μLPBFed samples, accompanied with smaller grain size, higher density of low-angle grain boundary (LAGB) and geometrically necessary dislocation (GND). μLPBF creates a cellular microstructure with smaller cell size and cell wall thickness compared with cLPBF. The yield strength of μLPBFed samples is marginally lower than cLPBFed ones, which is dominated by the difference of compositional microsegregation in the cellular structures. Both cLPBFed and μLPBFed samples

show a strong anisotropy in terms of yield strength, ductility and deformation behavior. The distortion measurement of the printed cantilever design suggests a lower level of macroscopic residual stresses in the μLPBFed samples due to the smaller molten pool and more thermal cycles. Moreover, the microstructure, mechanical properties and distortion of μLPBFed samples remain at the same level with variation of laser power and scanning speed. Overall, better surface finish, finer microstructure, more desirable mechanical properties and smaller part distortion can be obtained by μLPBF.

Key words: micro laser powder bed fusion (μLPBF); stainless steel; microstructure; mechanical properties; distortion

1. Introduction

Metal Additive Manufacturing (AM) technology has been developing rapidly these years due to its strong capability in producing near-net-shaped complex structural components directly ready for industrial applications, which is difficult or impossible to achieve by conventional fabrication technologies [1]. Among various metal AM technologies, laser powder bed fusion (LPBF) is often employed for complex part fabrication, thanks to its noticeable ability of producing components with low porosity and high accuracy [2, 3]. Modern LPBF systems usually adopt a focused laser beam with spot size approximately ranging from 50 to 100 μm, metallic powders with size between 10 and 60 μm and layer thickness varying between 30 and 50 μm. [1, 4]. Commonly, a surface roughness (Ra) of 7~20 μm [1] and a minimum feature size of ~ 200 μm [5-7] can be realized by these conventional LPBF (cLPBF) systems. However, with the trend of product miniaturization and increasing requirement on surface quality and geometrical accuracy, cLPBF system can no longer meet such demand. Hence, micro LPBF (μLPBF) system needs to be developed and introduced to the industry.

Generally, μLPBF can be realized via implementation of some essential modifications and improvements to get proper conditions [8], including refining the laser spot size (e.g., 25 μm or even smaller), improving the movement precision of building platform and using smaller metallic powders (e.g., 0~25 μm). Our research team has been dedicating into the development of μLPBF for fabrication of micro metallic components [9-11]. Recently, a μLPBF system has been further developed based on a refined laser system which can achieve laser beam diameter <= 25 μm and layer thickness <10 μm. The μLPBF system has been successfully used to fabricate different materials as reported in [10, 11]. To date, the relationships between process parameters, microstructures and properties for conventional LPBF of various materials have been intensively studied and reviewed [12-17]. However, these established data, information and knowledge related to the larger scaled LPBF cannot be directly scaled down and leveraged into the micro-scaled one. Thus, further and thorough studies on the μLPBF using different metals and alloys from different aspects of process determination, microstructures detailing and mechanical properties tailoring, etc. are crucially needed since the underlying mechanisms could be different. Besides, the differences in surface quality, microstructure and mechanical properties caused by μLPBF and cLPBF are complicated and may not be simply caused by a single process parameter. The dominant factor and the underlying mechanisms of these differences in μLPBF and cLPBF should be, but have not yet been figured out.

Austenitic stainless steel 316L (SS316L) has been widely used in the industry due to its good mechanical properties, good wear resistance, excellent corrosion resistance, as well as low cost. SS316L is an easy-to-process material by LPBF, and numerous studies have been conducted to investigate its microstructure and mechanical properties [18-22]. In traditional processing technologies, the strengthening of steels typically comes together with ductility loss. In contrast, high strength and ductility of SS316L produced by LPBF can be obtained thanks to the hierarchical microstructure including grain structure, solidification cellular structures, and dislocations as

reported in [18-20]. The hierarchical microstructure dominates the mechanical properties, and both of them can be affected and tailored by varying process parameters. Niendorf et al. [21] reported that a high laser power of 1000 W accompanied with a layer thickness of 150 μm could result in a strong textured columnar coarse-grains and a lower yield strength but higher Young's modulus as compared with a 400 W laser and a layer thickness of 50 μm. Montero-Sistiaga et al. [4] compared 316L produced by LPBF with a 1 kW laser of 700 μm in spot size and a 400 W laser of 76 μm in spot size, finding that high power leads to an increase of morphological and crystallographic texture and coarsening of cells. Sun et al. [22] found that higher laser power brings about higher yield strength and elongation. Besides the microstructure and mechanical properties, other aspects like surface roughness and part distortion due to macroscopic residual stress are also affected by the LPBF process [23, 24]. It can be concluded that the reported results for cLPBF of SS316L could differ from each other due to different system conditions [25, 26]. Despite of this, they provide substantial knowledge for us to understand the underlying mechanisms of microstructures and mechanical properties. When scaling down to μLPBF of SS316L, the resultant differences in geometric, microstructural, and mechanical properties remain unknown, which warrants further investigation.

This work aims at better understanding the aspects including surface quality, microstructure, mechanical properties and part distortion of SS316L produced by the μLPBF as compared with cLPBF. The μLPBF in this work is characterized by a laser spot size of 25 μm and powder size of 5~25 μm, while in cLPBF they are 80 μm and 15~53 μm, respectively. To do so, the surface quality of as-printed parts is examined. The crystal structure and solidification cellular microstructure are compared, and the effects of μLPBF main process parameters, namely laser power and scanning speed, are studied. Tensile properties and deformation behavior are analyzed considering the effect of specimen orientation. A standard cantilever design is employed and printed to study the distortion induced by macroscopic residual stresses.

2. Materials and methods

2.1 Material and process

Austenitic SS316L powder produced by gas atomization technology provided by Beijing AMC Powder Metallurgy Technology Co., Ltd was used for fabrication. The chemical composition of the as-received powder is shown in Table 1. For μLPBF, finer powder with particle size of 5~25 μm (D_{50}=16.27 μm) was employed to improve the surface quality. Finer metal powder is necessary if micro-scale feature size of products by μLPBF is desired. One should also be aware of the powder flowability during reduction of the particle size, since finer powder tends to agglomerate due to larger specific surface area. The selected fine SS316L powder was tested with reasonable flowability, which ensures good manufacturability by μLPBF. In addition, cLPBF was utilized for comparison study, where common particle size of 15~53 μm (D_{50}=33.51 μm) was selected. Fig. 1 shows the Scanning Electron Microscope (SEM) images and the particle size distribution of the two kinds of powders.

Table 1 Chemical composition of as-received SS316L powder

Element	Cr	Ni	Mo	Mn	Si	P	S	C	O	Fe
wt. %	16.88	13.6	2.7	0.54	0.41	0.012	0.0063	0.0066	0.0875	Bal.
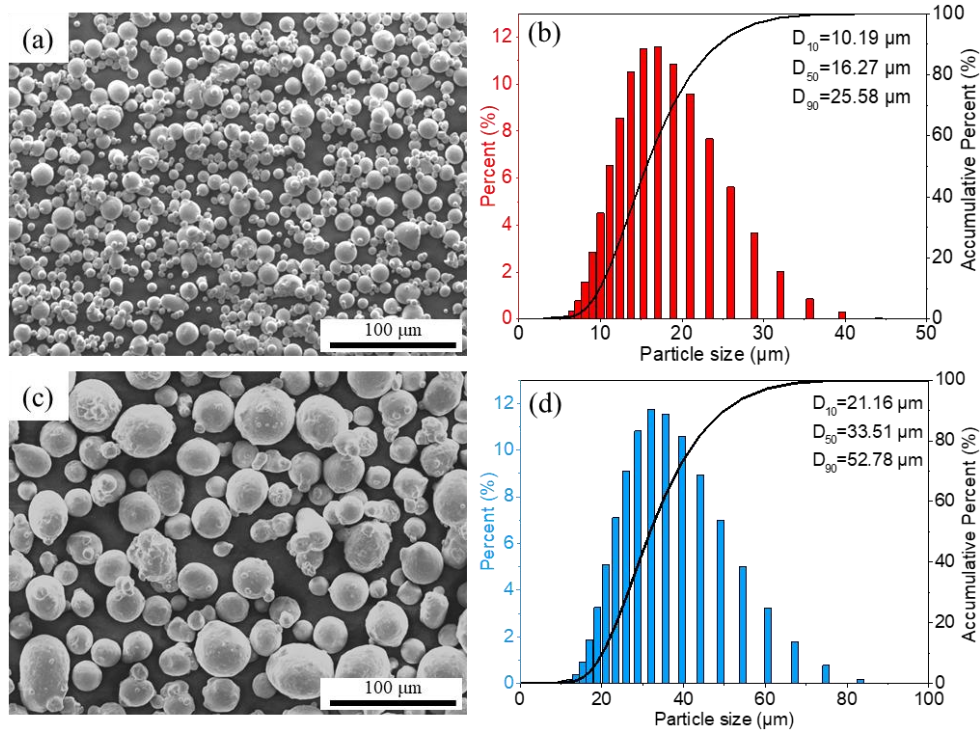
Fig. 1. SEM images and particle size distribution of as-received 316L powder for (a, b) μLPBF and (c, d) cLPBF.

A conventional LPBF machine and an in-house developed μLPBF one (Han's Laser M100) based on the same cLPBF model were employed for comparison study. The machine configurations are almost the same except for the laser system (laser spot size). Both machines are quite stable and can produce metallic parts with high repeatability. A continuous 500 W IPG fiber laser (λ=1.07 μm) with beam diameter of 25 μm and 80 μm are equipped in the two systems, respectively. The LPBF processes were conducted in N_2 gas atmosphere at an oxygen content lower than 500 ppm. The SS316L substrate was heated up to 80 °C before and during LPBF process to reduce thermal stress. Based on our previous parametric study [11], appropriate process parameters of cLPBF and μLPBF were selected. Different laser power (P) and scanning speed (V) combinations of μLPBF were chosen to study their effects on microstructure and mechanical properties. Table 2 shows the selected process parameter configurations for cLPBF and μLPBF. A 99.3% relative density or higher can be achieved with the selected parameters based on porosity examination. During

all LPBF processes, the commonly adopted hatch angle of 67 ° between every layer was set to reduce thermal residual stress since the subsequent vectors can avoid overlapping with previous patterns during rotation. Fig. 2 shows the building setup on the substrate with three types of samples: (1) cubes with dimensions of 5×5×5 mm for surface quality and microstructure evaluation, (2) horizontally (A0) and vertically (A90) placed cubes with dimensions of 57×10×10 mm, from which dog-bone shaped tensile specimen (Fig. 2(b)) with gauge dimension of 15×4×1.2 mm was cut by Electrical Discharge Machining (EDM), and (3) cantilever for distortion measurement after EDM [24], with overall dimension of 80×8×7 mm and teeth of 0.6×5 mm fixed on a 3mm thick cantilever beam (Fig. 2(c)).

Table 2 Process parameter configurations for cLPBF and μLPBF

Process parameter	Laser power (P, W)	Scanning speed (V, mm/s)	Hatch spacing (H, μm)	Layer thickness (t, μm)	Remarks
cLPBF	220	950	100	40	EBSD, SEM, Tension A0/A90, Cantilever
μLPBF No. 1	50	770	50	10	EBSD, SEM, Tension A0, Cantilever
μLPBF No. 2	50	910	50	10	Tension A0
μLPBF No. 3	50	1000	50	10	EBSD, SEM, Tension A0/A90, Cantilever
μLPBF No. 4	55	1000	50	10	EBSD, SEM, Tension A0, Cantilever
μLPBF No. 5	65	1000	50	10	Tension A0
μLPBF No. 6	40	1000	50	10	Cantilever
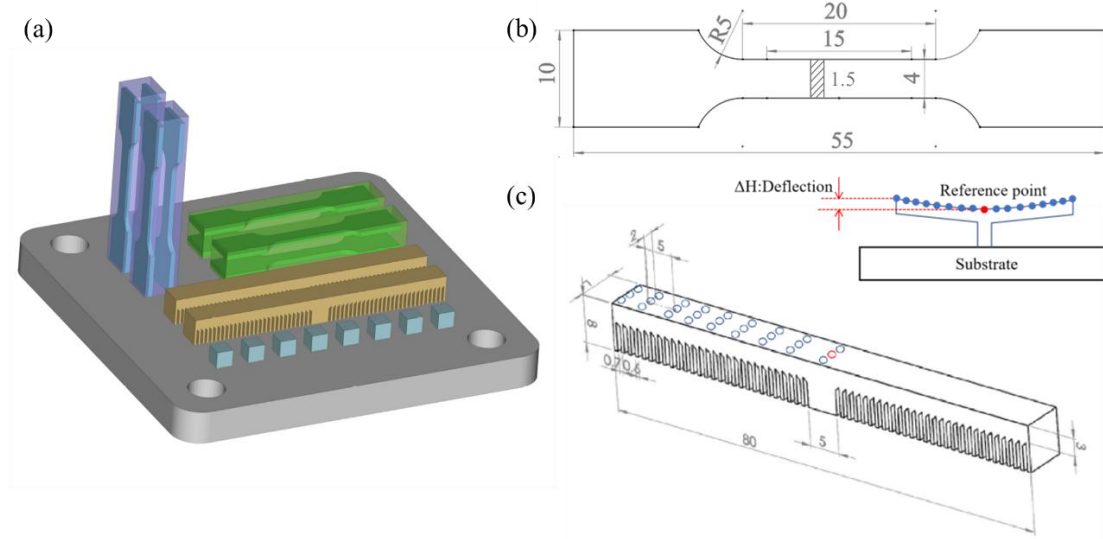
Fig. 2. (a) Printing setup, (b) geometry of tensile specimens and (c) geometry and measurement schematic of cantilever.

2.2 Characterization

SEM observations were conducted on JCM-6000PLUS and VEGA3 TESCAN to characterize the powder morphology, the surface quality, microstructure and the fracture surface of LPBFed samples. Surface roughness of as-printed samples were examined by 3D Laser Scanning Microscope (KEYENCE VK-X200). ImageJ software was used to process SEM image to measure the solidification cellular structure. It should be noted that the accurate cell size cannot be easily measured due to the cell geometry and random orientation. Therefore, the regions presenting near-equiaxed morphology were selected for cell size approximation. The average cell size was determined by measuring the cells positioned near the molten pool boundaries with at least 3 molten pools involved in calculation. Grain structure, texture and GND distribution of the as-printed samples were studied using a built-in Oxford Instruments Electron backscatter diffraction (EBSD) system at a step size of 0.5 μm on an area of 300×300 μm^2 and 500×500 μm^2 for μLPBFed and cLPBFed samples respectively. The raw EBSD data was analyzed using MTEX 5.3, which is an open Matlab toolbox for analyzing and modeling crystallographic features [27]. Grain boundaries (GB) are classified according to their misorientation angle into low angle

grain boundaries (LAGBs) and high angle grain boundaries (HAGBs), where the former range between 2 ° to 15 ° and the later are characterized by misorientation angle >15 °. The grain size is determined according to HAGBs. All GB fractions computed in this work are length fractions. The geometrically necessary dislocation (GND) density was estimated based on the function proposed by Pantleon [28], which has been successfully used to quantify the GND density of many alloys with different states [29-32]. The samples for microstructure characterization were mechanically grinded using sandpapers followed by polishing using a 0.05 μm grit silica solution, then chemically etched using aqua regia. Vicker hardness was measured on the FM-7E hardness tester with a load of 200g for 15s on each mechanically polished sample surface, and the average hardness was calculated by using the values of 10 indents, excluding the maximum and minimum values. Room-temperature uniaxial tensile tests were conducted on Instron E10000 at a speed of 0.9 mm/min (strain rate $\sim 10^{-3}$ s^{-1}) with a video extensometer recording the tensile strain of the gauge portion of the tensile specimen. Before tensile testing, the specimens were mechanically grinded using sandpapers to eliminate the effect of rough surface. Three tensile tests were conducted for each specimen to ensure the repeatability of the results. The distortion of the cantilever after EDM was measured by Coordinate Measuring Machine (CMM), namely, FaroArm Platinum (2.4m) with a precision of ±0.03 mm. A total of 51 points (24 points on each side and 3 points on the center of cantilever were measured (Fig. 2(c)). The deflection was obtained by the relative height difference between the reference point (red) and other points (blue) measured on different locations of a cantilever. The height of three points in each row were averaged to show the deflection in the length direction. Both sides of cantilever were averaged to eliminate random errors.

3. Results

3.1 Surface quality characterization

Fig. 3 shows the SEM images of the part surfaces printed by cLPBF and μLPBF,

where the top surfaces and side surfaces were characterized and surface roughness were measured. The scanning direction of laser tracks can be clearly observed on the top surfaces. The distance between adjacent laser tracks is equal to the predefined hatch distance, namely 50 μm and 100 μm for μLPBF and cLPBF, respectively. There are significantly more un-melted powders adhered on the side surfaces than those on the top surfaces for both LPBF processes. The surface roughness Ra of both top and side surfaces (3.40 and 5.66 μm) of μLPBFed samples is lower than that of cLPBFed ones (7.63 and 9.47 μm). The surface roughness obtained by μLPBF in this work is lower than that in some other studies who used conventional systems [23, 33], which is attributed to the fine laser beam and fine powder we used. Therefore, the fine laser beam equipped on μLPBF system can not only achieve smaller minimal feature size, but also ensure better surface finish, providing great potential for precision engineering applications.
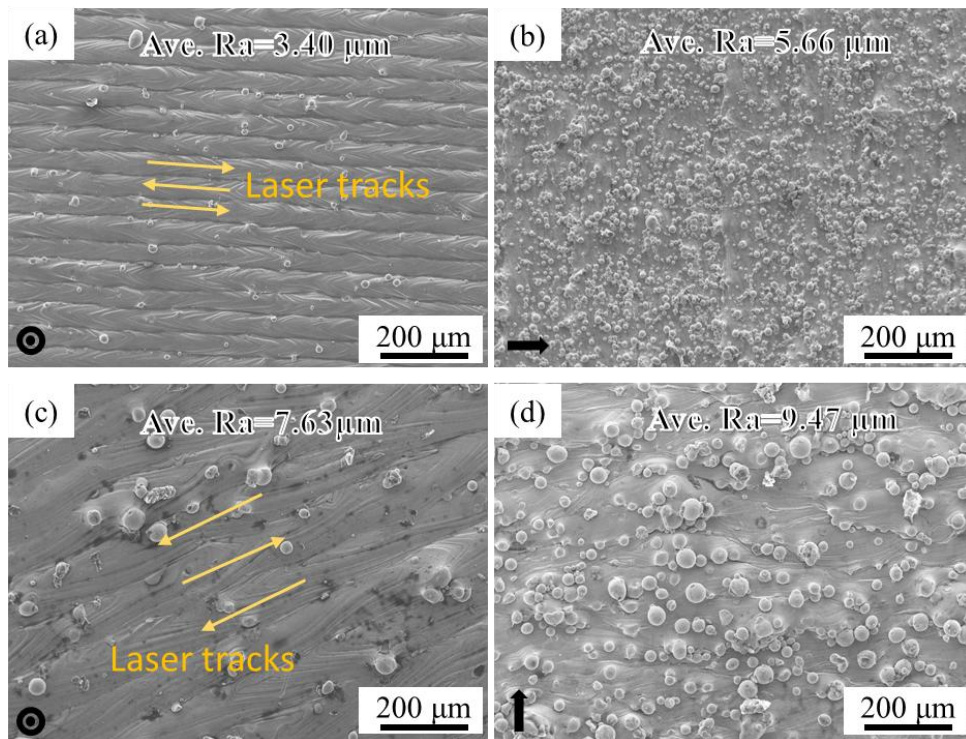
Fig. 3. SEM surface characterization of (a, b) μLPBF and (c, d) cLPBF produced parts; (a, c) top surfaces and (b, d) side surfaces; the bottom-left black arrows denote the building direction.

3.2 Crystal structure

Fig. 4 shows the EBSD results of grain orientation maps and inverse pole figures (IPF) of as-printed SS316L parts by cLPBF and μLPBF. A larger area of cLPBFed sample of 500 μm × 500 μm is selected for EBSD examination due to its larger grain size, and an enlarged area of 300 μm × 300 μm is used for direct comparison with μLPBFed counterparts, as shown in Fig 4(a, b). A <110> texture along building direction (BD) with different intensities for all samples is visible in the grain orientation maps, which was also observed in [34-36]. According to the IPFs (Fig. 4(f)), the intensity of the texture <110>//BD for cLPBF is 2.1, weaker than the texture intensity of all over 3.7 of μLPBFed samples (Table 3). Some additional <100>//BD textured grains can be observed in all samples, which has a higher intensity in cLPBFed sample. From morphology point of view, the grains of these LPBFed parts are very irregular compared with conventional fabricated materials. Large columnar grains along BD accompanied with some small equiaxed grains are formed. Interestingly, some Chevron-shaped grains are observed in cLPBFed sample (see Fig. 4(b)), and similar Chevron patterns were observed in [36]. Fig. 4(g) shows a broad grain size distribution extracted from EBSD raw data. The average grain size (equivalent grain diameter) defined by HAGB is computed as 10.31 μm, 8.15 μm, 7.16 μm and 7.87 μm (Table 3), corresponding to Fig. 4 (b, c, d, e). It is concluded that larger laser beam with higher power produces larger grains (cLPBF), and small variation of laser power or scanning speed for μLPBF does not significantly affect the grain size.

Fig. 5(a~d) plot the grain boundary (GB) network computed from the raw EBSD data on corresponding samples. Fig. 5(i) shows the fraction and length density of LAGB and HAGB. The EBSD measurement shows a large fraction of LAGBs formed in the cLPBFed and μLPBFed SS316L, which is a typical feature of LPBFed SS316L [18, 35]. Among all μLPBFed sample, LAGBs account for a same level, about 70% of the

total GBs (Table 3). This suggests that the small variation of laser power and scanning speed does not significantly affect the GB formation. In comparison, cLPBFed sample contains a relatively lower fraction of LAGBs of ~60.6%. In addition, the length density of GBs is calculated by total LAGB/HAGB perimeter divided by the observed area. The lower length density of GBs for cLPBF is consistent with its larger grain size.

Fig. 5(e~h) show the GND maps computed from the raw EBSD data on corresponding samples. The dark colors (red and orange) correspond to high dislocation density, while the light color (green) represents low dislocation density. It is clear that the GND is distributed heterogeneously across the microstructures. It shows a high consistency with the LAGB distribution, with GND mainly located along LAGBs. The dark colors are predominantly present in all μLPBFed samples, suggesting a high dislocation density. In contrast, the overall GND density becomes much lower in cLPBFed sample, corresponding to its larger grain size and less LAGBs. Fig. 5(g) illustrates the frequency distribution histograms of all discrete GND density measurements. Similar GND density distribution was also reported in [29]. It should be pointed that before quantifying the GND density, the uncertainty of GND measurement by EBSD needs to be considered. The noise floor of GND density is estimated using the method proposed by Wilkinson et al. [37] as follows:

$$\rho_{noise} = \frac{\delta}{b\Delta x} \tag{1}$$

where δ is uncertainty in the EBSD measurement (~0.1°, upper-bound) [31]. b and Δx are Burgers vector (0.2546 nm) and step size (0.5 μm), respectively. Therefore, the estimated noise floor of GND measurement is calculated to be 7.86×10^{12} /m^2. It is confirmed that the GND measurements of all pixels are larger than the noise floor. From the extracted results, the GND density for cLPBFed sample is 9.84×10^{13} /m^2, about half of that for μLPBFed samples, i.e., 1.77×10^{14} /m^2, 1.75×10^{14} /m^2, and 1.70×10^{14} /m^2 for sample No. 1, No. 3 and No.4, respectively (Table 3). The GND density across the LAGBs and within grains interiors are in the order of 10^{15} and

10^{13}-10^{14} /m^2 respectively, similar to the calculation in [29]. Similar to other microstructural features, the GND density is almost the same among μLPBFed samples. Moreover, it is found that the ratio of GND density and LAGB length density is almost constant for all samples from cLPBF and μLPBF, indicating the two features (LAGB and GND) are highly correlated.
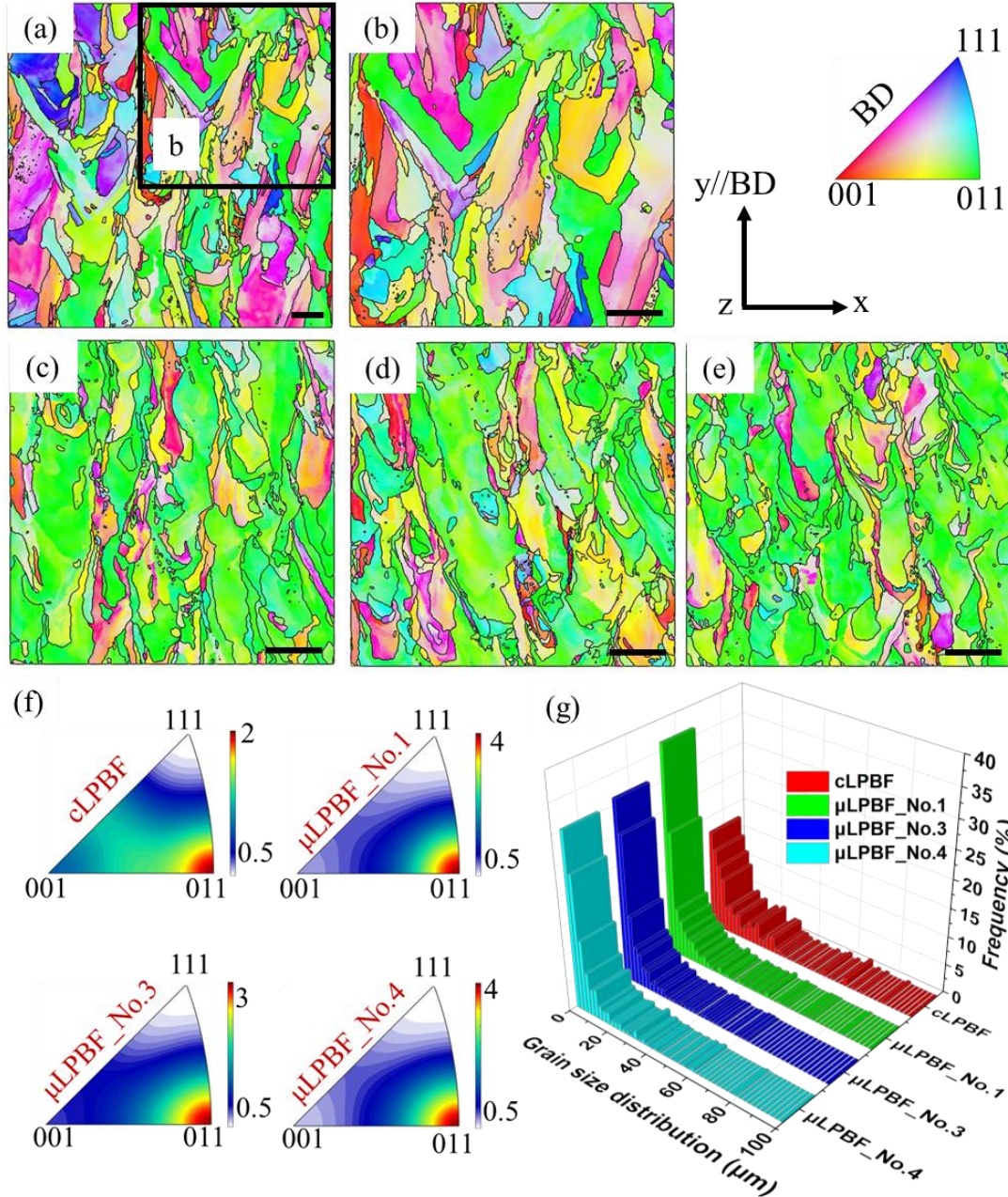
Fig. 4. Grain orientation maps of as-printed 316L parts of: (a, b) cLPBF and (c, d, e) μLPBF (for No. 1, No. 3, No. 4 respectively); (f) Inverse pole figures (IPF) along BD; (g) Histogram of grain size distribution; The scale bar is 50 μm; BD denotes the
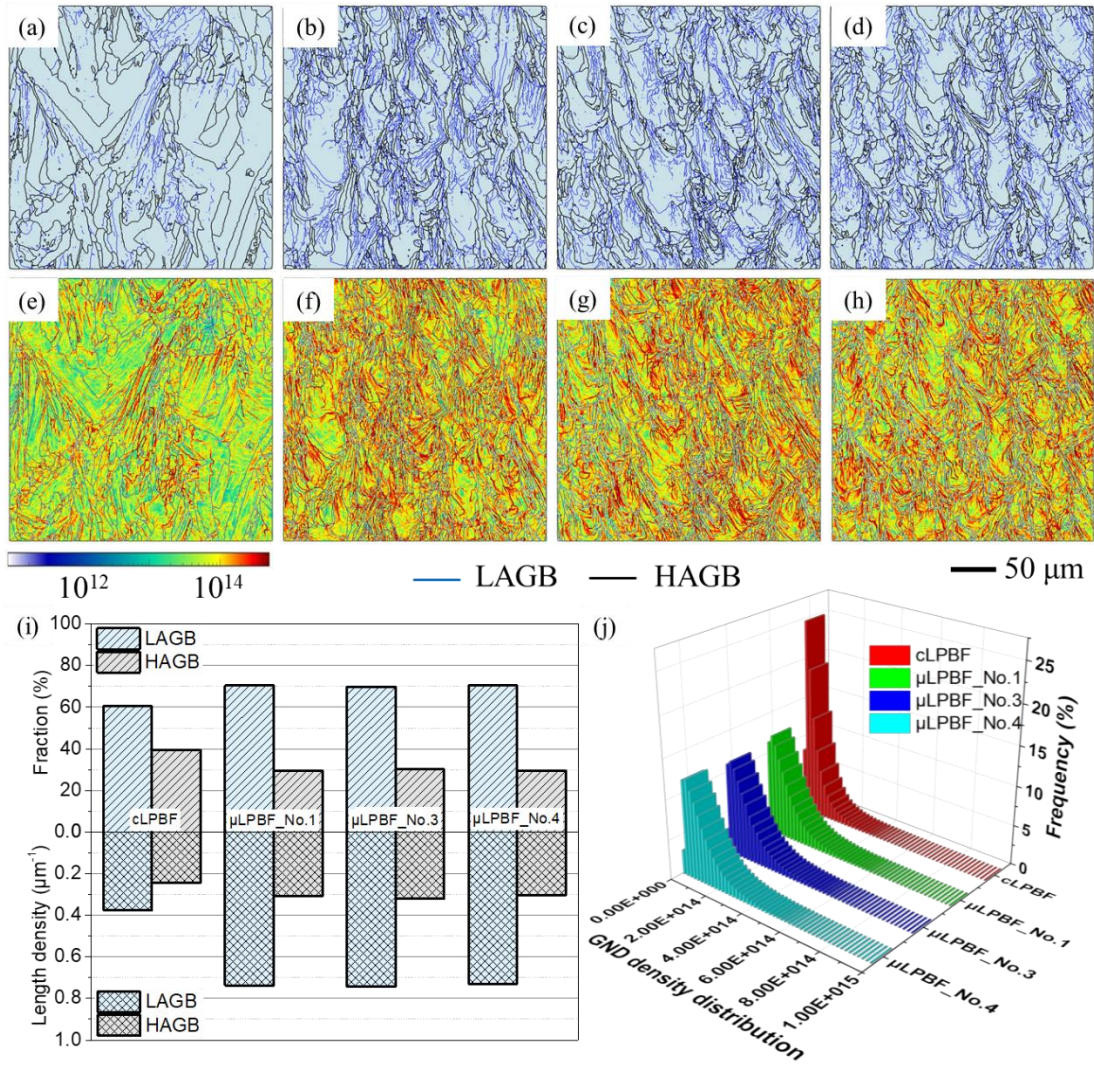
Fig. 5. (a-d) GB maps and GND (e-h) maps of as-printed 316L parts by cLPBF (a, e) and µLPBF (No. 1(b, f), No. 3(c, g), No. 4 (d, h)); (i) Histogram of fraction and length density of GBs; (j) Histogram of GND density distribution.

Table 3 Statistics of EBSD results of as-printed cLPBF and µLPBF SS316L

	cLPBF	µLPBF_No.1	µLPBF_No.3	µLPBF_No.4
Maximum <110>//BD texture intensity	2.1	4.3	3.7	4.3
Grain size (µm)	14.35	8.15	7.16	7.87
Length density (LAGB/HAGB, µm⁻¹)	0.38/0.25	0.74/0.31	0.74/0.32	0.73/0.31
Fraction (LAGB/HAGB, %)	60.6/39.4	70.5/29.5	69.8/30.2	70.5/29.5

GND density (m^{-2})	9.84×10^{13}	1.77×10^{14}	1.75×10^{14}	1.70×10^{14}

3.3 Solidification cellular structure

Fig. 6 shows the representative SEM observation of typical solidification cellular structure of LPBFed SS316L parts. Fig. 6(a, d, e and f) are the low-magnification images for cLPBF and μLPBF, respectively. Yellow dashed lines decorate the molten pool boundaries. Some high angle grain boundaries (HAGBs) perpendicular to the molten pool boundaries can be distinguished after etching as highlighted by blue lines. The molten pool in cLPBF is much larger than that in μLPBF, which is caused by the larger laser beam diameter.

At finer scale (Fig. 6(b, g, h and i)), solidification cellular structure is observed within the molten pools. The white contrast of cell walls mainly comes from microsegregation due to rapid solidification, with chromium and molybdenum enriched on the cell walls [18, 38]. In a 2D map, the honeycomb-like cell arrays demonstrate a mixed pattern with polygons or long parallel laths due to different growth directions. In terms of cell size, as measured in Fig. 6(c), cLPBF creates a cell size of 866.8 nm in average, over two times larger than μLPBFed ones, with 389.2 nm, 309.2 nm and 429.2 nm for sample μLPBF No. 1, No. 3 and No. 4, respectively. Sample μLPBF No. 3 has the smallest cell size. In all of our cases, the thickness of the cell walls ranges approximately from 40~130 nm, of similar level reported in [18]. The largest cell wall thickness of 128.6 nm is measured for cLPBFed sample, suggesting a more significant compositional segregation. The enlarged images (Fig. 6(j, k and l)) show the presence of precipitates both on cell walls and in the cell interior. The precipitates are mainly detected as Mn-enriched SiO$_2$ [18, 39]. These spherical precipitates are measured with diameter lower than 50 nm.
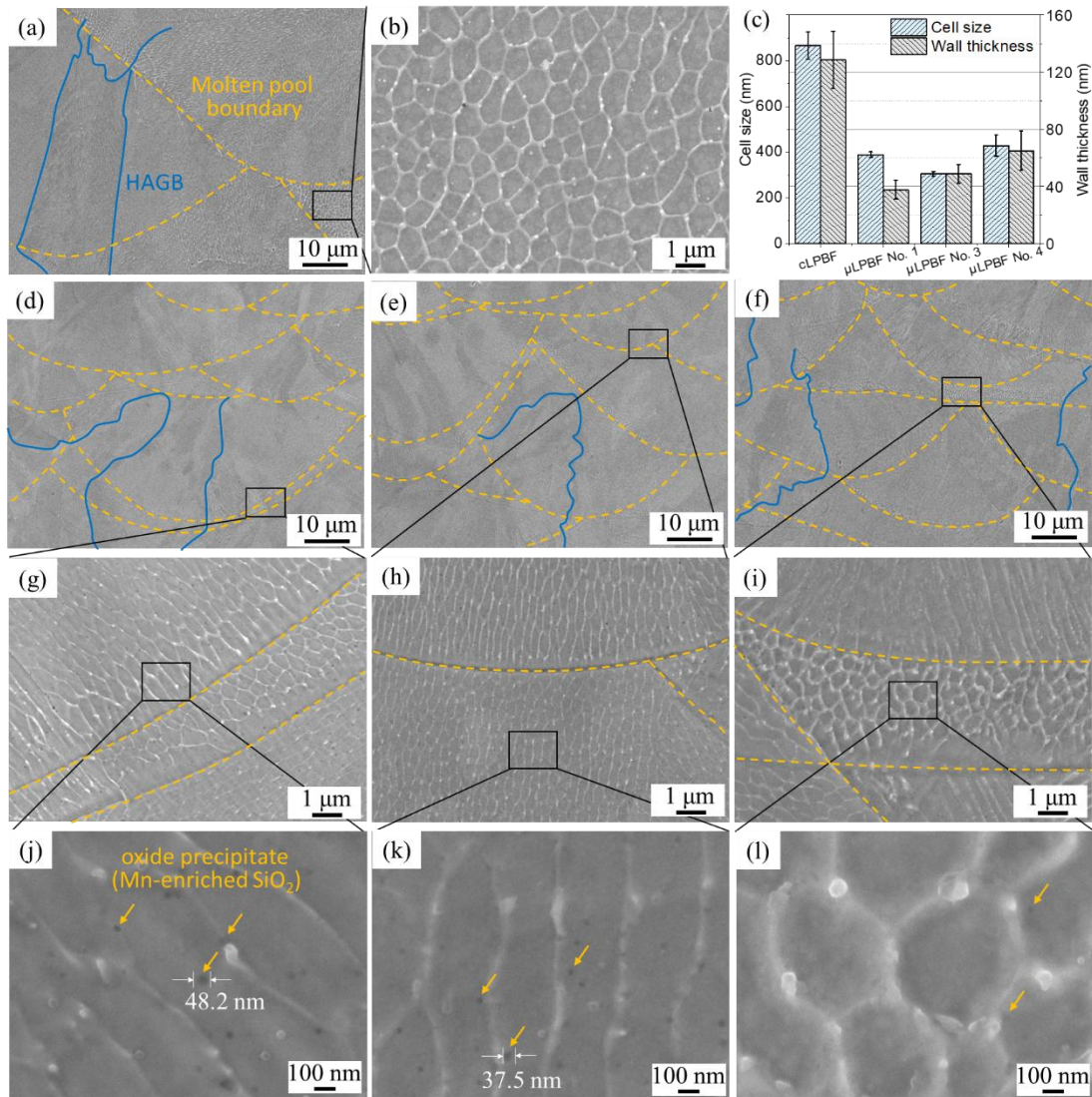
Fig. 6. Solidification structure of the as-printed SS316L parts by (a, b) cLPBF and (d~l) μLPBF (No. 1 (d, g, j), No. 3 (e, h, k) and (f, i, l) No. 4 respectively); (c) Histogram of cell size and wall thickness measurement for as-printed parts.

3.4 Mechanical properties

Fig. 7 shows the results of room-temperature tensile tests of as-printed 316L parts produced by cLPBF and μLPBF. Fig. 7(a-d) provide the representative engineering/true stress-strain curves. Fig. 7(g and h) summarize the mechanical properties including 0.2% yield strength, ultimate tensile strength, fracture elongation and Vicker hardness. Table 4 lists the average values of the properties of SS316L parts by cLPBF and μLPBF.

Among the μLPBFed samples (Fig. 7(a, b and g)), the process parameter of μLPBF No. 3 brings about the best combination of strength and ductility. The other four sets of μLPBF parameters produce the same level of tensile properties, with yield strength about 500 MPa, ultimate strength 815 MPa, fracture strain 32%. The difference of hardness for all μLPBFed samples is not evident (all around 200 HV). In this case, sample μLPBF No. 3 is selected to compare with cLPBF in terms of tensile properties. In Fig. 7(c, d), a fluctuating yielding behavior is observed for μLPBFed sample while not for cLPBFed one. In addition, it is interesting to find that for both directions (A0 and A90) the strengths of cLPBFed samples are higher than those of μLPBFed ones, while their elongations are comparable. On the other hand, the vertical tensile specimens (A90) for both LPBF processes exhibits lower yield strength but higher elongation compared with their A0 counterparts.

Fig. 7(e) provides the evolution of normalized strain hardening rate (θ) as a function of flow stress for cLPBFed and μLPBFed samples with different directions. θ is calculated as follows:

$$\theta = \frac{1}{\sigma}\left(\frac{d\sigma}{d\varepsilon}\right) \tag{2}$$

where σ and ε are flow stress and true strain, respectively. The bottom light-blue region indicates the post necking period, which starts when $\theta = 1$ [38]. The excellent strength-ductility combination of LPBFed 316L can be reflected by the continuous and steady strain hardening ability at high stresses, which could lead to an excellent uniform elongation [18]. Lower strain hardening rate with small change after yielding for A90 samples by cLPBF and μLPBF is observed, presenting steadier work hardening capability compared with A0 samples, which has a higher strain hardening rate upon yielding. The similar change of θ for both cLPBF and μLPBF with same direction indicates a similar strain hardening capability.

To better understand the deformation behavior, instant work hardening exponent, n,

was utilized to analyze the strain hardening capability of the material. Fig. 7(f) exhibits the evolution of *n* as a function of true stress. The instant work hardening exponent, *n*, is given by

$$n = d(ln\sigma)/d(ln\varepsilon) \tag{3}$$

where *n* is firstly introduced in the formula known as Hollomons equation [40]. Most metals have a *n* value ranging from 0.1 to 0.5. In this work, all involved samples have a *n* value between 0.03 and 0.45. During plastic deformation, the exponent *n* scales from a minimum to a maximum. For same tensile direction, cLPBFed samples have a slightly lower discrepancy between minimum and maximum *n* than μLPBFed samples. On the other hand, for both cLPBF and μLPBF, the exponent *n* of A90 samples increases rapidly with increasing stress, till a higher maximum value of about 0.43 and 0.45, compared with the lower maximum value of 0.24 and 0.3 for A0 samples of cLPBF and μLPBF, respectively. The evolution of *n* again suggests a comparable strain hardening capability between cLPBFed and μLPBFed samples, and A90 samples have better strain hardening capability than A0 samples.

Fig. 8 presents the SEM observations of fracture surfaces of as-printed cLPBF and μLPBF. Both cases indicate a typical ductile fracture, with small dimples observed. The fracture mechanism is related to nucleation, growth and coalescence of micro voids during plastic deformation. It is interesting to note that the dimple size is comparable or to some extent smaller than the solidification cell size. Similar to the SEM observation of cellular structure, the dimple size for cLPBF is slightly larger than that for μLPBF, about 400 nm and 200 nm in average, respectively. From the rough fracture observed in Fig. 8(b), different oriented solidification cells can be recognized, which result in a high fracture surface area, proving large energy absorption before fracture accompanied with a high elongation. It suggests that the cellular structure plays an important role in affecting the deformation process and the formation of micro voids. In addition, pores with size comparable to the as-received powder are observed, proving the existence of inherent process induced pores.
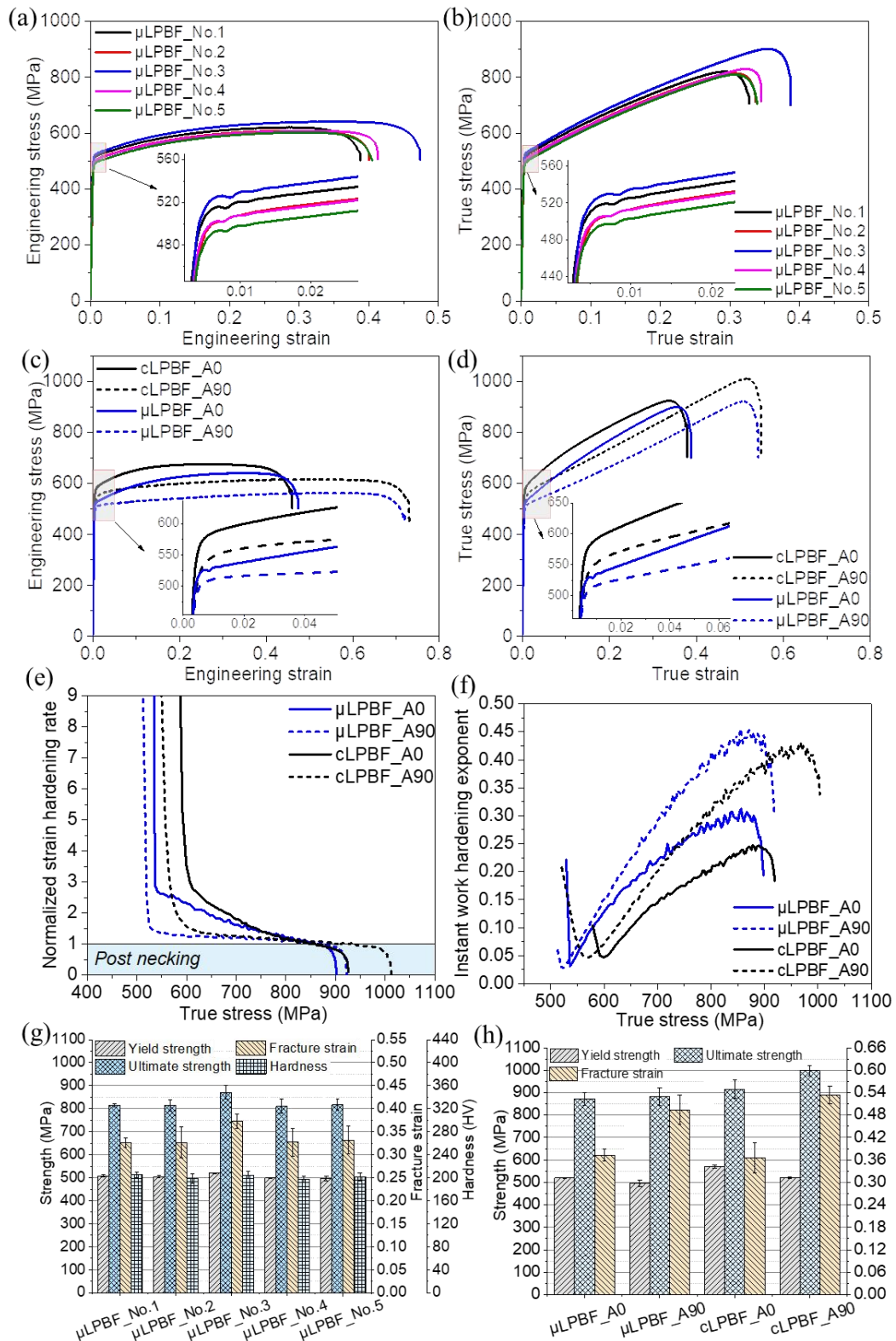
Fig. 7. Representative (a, c) engineering and (b, d) true stress-strain curves SS316L

parts by μLPBF and cLPBF; (e) normalized work hardening rate; (f) instantaneous

work hardening exponent; (g, h) histograms of mechanical properties including yield

strength, ultimate strength, fracture strain and hardness.

Table 4 Values of properties of SS316L parts by cLPBF and μLPBF

Samples	True yield strength (MPa)	True ultimate strength (MPa)	Fraction strain	Hardness (HV)
μLPBF_No.1 (A0)	508.5±5.0	815.8±6.7	0.327±0.01	205.3±4.7
μLPBF_No.2 (A0)	504.2±5.7	815.2±23.2	0.327±0.03	199.0±7.9
μLPBF_No.3 (A0)	519.4±3.2	871.5±28.9	0.373±0.02	204.5±6.2
μLPBF_No.4 (A0)	499.1±1.8	810.5±31.3	0.327±0.03	197.8±5.5
μLPBF_No.5 (A0)	496.8±10.3	817.4±24.1	0.332±0.03	201.7±6.6
μLPBF_No.3 (A90)	496.0±14.2	881.8±39.7	0.494±0.04	202.7±5.1
cLPBF_A0	570.3±7.0	914.8±40.6	0.366±0.04	219.5±4.3
cLPBF_A90	521.7±3.66	997.3±23.9	0.534±0.02	215.6±3.6
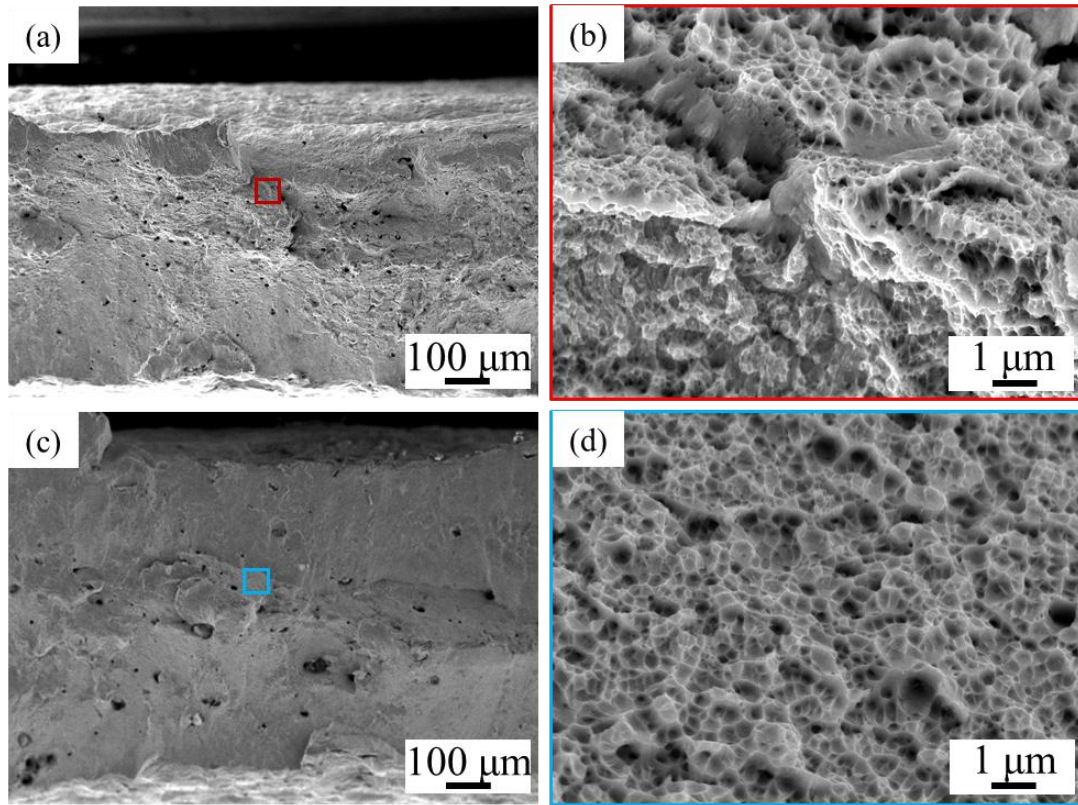
Fig.8. SEM observations of fracture surfaces of as-printed 316L tensile specimens fabricated by (a, b) μLPBF and (c, d) cLPBF.

3.5 Cantilever distortion

Due to the constraints of substrate, the deflection of cantilever after EDM reflects the macroscopic residual stress produced by LPBF manufacturing process. As the

cantilever specimens were cut from substrate, different levels of distortion were measured in the specimens of cLPBF and µLPBF. Fig. 9 shows printed cantilevers and the average deflection of both sides of cantilevers fabricated by cLPBF and µLPBF. cLPBFed cantilever has a 1.201 mm upward deflection along z-axis at the end of cantilever, suggesting a larger distortion than µLPBFed cantilevers. The different parameters of µLPBF result in deflections in the range of 0.845mm to 0.878 mm along z-axis. Among the four groups of µLPBF process parameters, No.1 has the maximum deflection due to the maximum energy input caused by the lowest scanning speed. No.4 and No.3 respectively have the second and third largest deflection, which are 0.863 mm and 0.853 mm respectively at the tip of cantilever. Comparing the curves of No.3 and No.6, it is obvious that No.6 has a lower deflection reading, which is attributed to the lower laser power.
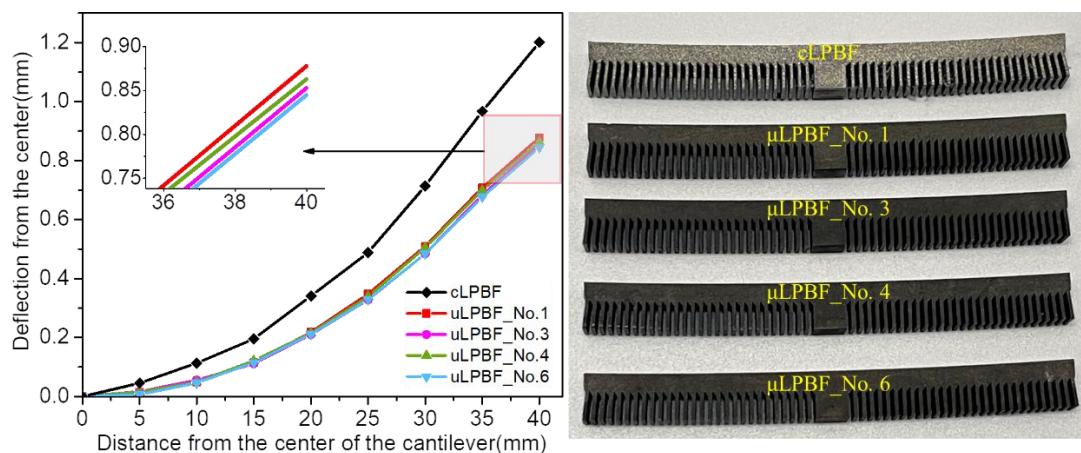
Fig. 9. Deflection of cantilevers produced by cLPBF and µLPBF.

4. Discussion

4.1 Surface quality and microstructure

a. Surface roughness

The surface roughness of the top and side surfaces is affected by the adhered powders and the molten pool. It can be readily understood that the horizontal layers can be fully melted by high energy density of the laser beam. The adhered powders on the final top surface can be attributed to the splashed powders, which cannot be melted

due to the fast cooling rate of the molten pool. While the side surface is always exposed to the powder sink, and a large number of powders can be partially melted and captured at the end of the laser track. As a result, the side surface roughness is higher than top surface roughness. Powder size also influences the surface roughness. It was found that the larger powder size could deteriorate surface quality, since the maximum surface grooves are significantly increased [41]. In comparison, fine particles can be more easily melted, contributing to the high part density, process productivity and surface quality [42]. Thus, the finer powder used in μLPBF is a superior feature compared with cLPBF. Besides powder, the molten pool also affects surface roughness. For cLPBF, the larger laser beam creates larger volume of molten pool, which can promote a phenomenon known as "balling" due to surface tension forces on the molten pool surface [43]. Balling effect increases surface roughness, especially affects the side surface, because of the balling scattering direction to the side of molten pool instead of top side [44]. The larger molten pool and larger powder size in cLPBF lead to a higher surface roughness compared with μLPBF as a result.

b. Crystal structure

Since both <110> and <100> directions are the easy growth directions in FCC materials, the <110>//BD texture is commonly reported for LPBF of SS316L [34-36], and the <100>//BD has also been reported in some cases [4, 19, 45]. The texture formation is governed by solidification conditions including thermal gradient and growth rate [46], which can be tailored by manipulating the process parameters such as laser power, scanning strategy, etc. ~~Niendorf et al. [21] found that a lower laser power produces a <110> texture, whereas a higher power generates a <100> texture.~~ The hatch angle of 67 ° is widely accepted due to its effectiveness in creating a random crystal orientation, whereas it is also reported the rotational scanning strategy cannot eliminate the formed texture especially along BD [47]. In this work, although hatch angle of 67 ° is used, it is interesting to find that the larger laser beam with higher power (cLPBF) leads to a weaker <110> texture, while the fine laser beam

with lower power (µLPBF) creates a stronger <110> texture. This can be explained by the fact that the larger molten pool with the lower cooling rate offers more opportunities for the competitive growth of grains with different crystallographic orientations. As a proof, the chevron-shaped grain formed in cLPBFed sample is attributed to the competition between heterogeneous nucleation and the epitaxial growth [36]. In addition, the strong Marangoni effect and high recoil pressure may exist in the larger molten pool in cLPBF, which result in strong convection flow and complex heat flux direction, and further promote the formation of the irregular grains with arbitrary orientations [22, 48]. As a result, the grains in cLPBF are weakly textured, while preferred grain growth with <110> aligned with BD are dominated in µLPBF because of the relatively smaller molten pool and its high cooling rate. On the other hand, the columnar grains formed in all samples are the result of epitaxial solidification, leading to continuous growth of sublayer grains along building direction penetrating several layers. For µLPBF, the smaller layer thickness of 10 µm allows the grains below several layers to preferentially grow with the optimal direction. The epitaxial growth of grains with the preferred crystallographic orientation dominates the solidification process in µLPBF, finally leading to a stronger texture [1]. For grain size, the larger molten pool is responsible for the larger grain size in cLPBFed samples due to lower cooling rate which is estimated in the following subsection.

c. Cellular structures, LAGBs and dislocations

Solidification cellular structure is commonly reported in Al-based, Co-based and Fe-based alloys fabricated by AM [49]. Cellular structures form as a result of localized heating and rapid cooling rate of LPBF [50]. The localized thermal gradient and cooling rate within individual molten pool determines the growth direction and size of the cells. Even within a specific molten pool, different oriented cell arrays can be created due to the curved molten pool boundary. The elongation direction of the cells is confirmed along <001> crystallographic directions [38, 51, 52]. In this work,

cLPBF process produces larger cell size than that of μLPBF. This is caused by the larger molten pool in cLPBF, accompanied with lower cooling rate which promotes cell growth. Besides, it is found that higher scanning speed and lower laser power (see Fig. 6(d, e, f)), namely higher cooling rate, favors smaller cell size. Therefore, among μLPBF produced cellular structures, sample No. 3 has the smallest cell size. Actually, the relationship between cellular spacing λ (μm) and cooling rate T (K/s) for austenitic stainless steel can be empirically approximated as follows [46, 53]:

$$\lambda = 80 \cdot T^{-0.33} \tag{4}$$

The cooling rate for cLPBF and μLPBF (No. 3) is estimated to be 9.02×10^5 and 2.05×10^7 K/s, respectively. The calculated cooling rate is well consistent with the values provided by prior arts of AM technologies, within the rage of 10^5 to 10^7 K/s [54]; while that for μLPBF is quite high, mainly attributed to its special fine laser beam. Therefore, ultrafine solidification microstructures can be expected using such μLPBF system, and microstructure control can be realized by manipulating the process parameters to optimize mechanical properties.

The cell walls are decorated with chemical segregation and oxide precipitates. In addition, the high density of dislocations is another particularly important feature of the cellular structures, as observed in [18, 22, 34, 38, 51, 55-58]. The dislocation cells are not the same as conventional ones since they overlap with dendritic microsegregation profiles [18, 51]. It has been confirmed that there is almost no misorientation between one cell to another in a "packet" of specific oriented cells [51]. Thus, the dislocations walls do not necessarily comprise GNDs, instead they could be grouped into statistically stored dislocations (SSDs). Bertsch et al. [51] recently revealed that the source of dislocation walls in AM materials is the deformation induced by thermal expansion and shrinkage in a constrained medium, and the dislocation structure development and density could be influenced by cooling rate, thermal gradient and heating/cooling cycles. Since μLPBFed sample experiences more heating/cooling cycles due to the smaller layer thickness (10 μm) and the higher

strain localization for the smaller molten pool, the density of the tangled dislocations in μLPBFed samples could thus be much higher than that in cLPBFed sample. Moreover, the empirical relationship between dislocation density on the cell walls (ρ_{dis}) and the cell size (d) can be expressed as [19]:

$$d = K_{dis} \, \rho_{dis}^{-1/2} \tag{5}$$

where K_{dis} is an arbitrary constant. Therefore, the smaller cell size of μLPBFed samples indicates a higher density of dislocations on the cell walls.

Besides the dislocations tangled on the cell walls, the AMed SS316L is also featured by a high density of GNDs, which are highly correlated to the LAGBs. The LAGBs are formed as a result of accumulative misorientation caused by coalescence of cells or dendrites as they grow [59]. According to our EBSD results, numerous LAGBs (over 60%) are formed in all as-printed samples. Similar findings have also been reported in [35, 38]. By comparison, the fraction or length density of LAGB of cLPBFed sample is lower than that of μLPBF. This can be explained by the difference of molten pool in the two conditions. Firstly, the molten pool size of cLPBF is much larger than that of μLPBF, definitely leading to the difference in the size of grain or sub-grain due to the grain growth confined by the molten pool boundary. Secondly, the curvature of the molten pool boundary in μLPBF is larger, which means the direction of thermal gradient frequently changes along the molten pool boundary. In contrast, the molten pool boundary for cLPBF is wide and flat, promoting cell growth with less misalignment formed. As a result, in μLPBF, the accumulative misorientation caused by the coalescence of the cells is widespread within the grains, accompanied with a higher density of LAGBs. These regions are rich in GNDs, which are required to accommodate the localized lattice misorientation. As a result, the GND density for cLPBF is lower than μLPBF accordingly, and same levels of GND density are detected among μLPBFed samples with different parameters.

4.2 Mechanical properties and deformation behavior

a. Yield strength

The yield strength of LPBFed metals is highly related to the thermal cycles and the resultant microstructures. According to the typical microstructure by LPBF, the yield strength mainly results from various strengthening mechanisms including grain boundary strengthening, composition strengthening, precipitate strengthening and dislocation strengthening. To comprehensively understand the strengthening mechanisms of LPBFed materials, the dominant strengthening factors need to be identified. Our tensile tests suggest that the yield strength of cLPBFed samples is slightly higher than that of μLPBF, by 50.9 and 25.7 MPa for the two direction A0 and A90, respectively. The difference of the yield strength should be attributed to difference of the as-printed microstructure.

The difference of the microstructure mainly exists on the grain size, cellular structure and dislocations. Specifically, the contribution of grain boundary strengthening σ_{GB} can be explained according to Hall-Petch relationship [60]:

$$\sigma_{GB} = K_{HP} \, D^{-1/2} \tag{6}$$

where D is the grain size, and K_{HP} is a material constant and can be assumed to be 327 MPa $\sqrt{\mu m}$ [61]. Thus, σ_{GB} for cLPBFed and μLPBFed samples with grain size about 10.31 and 7.16 μm can be calculated as 101.8 and 122.2 MPa, respectively. Dislocations are composed of GNDs near the LAGBs and SSDs tangled on the cell walls. Since the density of SSDs is difficulty to be directly measured, the strength contribution of GNDs is quantified for explanation. The Bailey-Hirsch relation is used to describe the dislocation strengthening effect [29, 62]:

$$\sigma_{Dis} = M\alpha G b\rho^{1/2} \tag{7}$$

where M is the Taylor factor derived from EBSD data to be about 3.05, α=0.23 is an empirical constant, and ρ is the dislocation density. b=0.2546 nm is the magnitude of Burges vector for austenitic SS316L, and G=73 GPa is the shear modulus [29]. The σ_{Dis} for cLPBFed and μLPBFed samples is calculated to be 129.0 and 172 MPa, respectively. The above calculation proves that strengthening effect of grain

boundary and GND for μLPBF is higher, while the obtained results show that cLPBFed sample has higher yield strength than uLPBFed sample, thus grain boundary and GND are not the dominant factors for the strength difference between cLPBFed and μLPBFed samples.

On the other hand, the nano oxide inclusions are reported to strengthen the LPBFed stainless steel [39]. By assuming an Orowan strengthening mechanism, Thomas et al. estimated an increase of shear stress of ~50 MPa caused by precipitate strengthening [38]. Cui et al. [29] and Smith et al. [62] predicted a precipitate strengthening effect of 11.7~14.2 MPa and 20~28 MPa, respectively. Therefore, the precipitate strengthening is limited. And the intrinsic strength caused by friction stress for both samples could be the same. Overall, it can be concluded that the cellular structure, which is composed of compositional microsegregation and dislocation cells, is responsible for the strength difference between cLPBFed and μLPBFed samples.

However, it is difficult to differentiate the strengthening effect from compositional microsegregation and dislocation cells. On the one hand, the estimation about the contribution of dislocation cells (SSDs) is significantly varying in current published studies [19, 29] due to the difficulty in SSD density measurement. According to previous empirical estimation, cLPBFed sample with larger cell size corresponds to a lower SSD density. Thus, the SSD strengthening is not the dominating factor for the strength difference. On the other hand, Smith et al. [62] estimated a significant strength contribution by compositional microsegregation. Combined with our SEM measurement, the much larger cell thickness (~128.6 nm) of cLPBFed sample suggests a more significant microsegregation, which could offer stronger barrier for initiation of dislocation slip and as a result a higher strengthening effect. Therefore, it is reasonable to conclude that the microsegregation strengthening effect is possibly responsible for the strength difference between cLPBFed and μLPBFed samples. Our findings suggest further exploration and quantification on the role of individual

feature in the cellular structure (compositional microsegregation and SSDs) on mechanical properties.

The small strength difference between the μLPBFed samples may also be related to the cellular structure, where sample No. 3 has the smallest cell size and moderate wall thickness and as a result a slightly higher yield strength. In addition, the anisotropic of yield strength is also observed, with A90 samples showing slightly lower yield strength compared with A0, which is related to the crystallographic orientation of the grains [63, 64]. The yield strength is determined by the activation of dislocation slip, and harder slip activation yields higher strength. The slip system will be activated once the stress along slip direction on the slip plane reaches the critical resolved shear stress. The relationship between yield strength σ_y and critical shear stress τ_s can be expressed as [65]:

$$\sigma_y = \frac{\tau_s}{m} = \frac{\tau_s}{cos\alpha \cdot cos\beta}$$ (8)

where α is the angle between the applied load and slip direction, β is the angle between the applied load and the norm of slip plane, and the product $m = cos\alpha \cdot cos\beta$ is the Schmid factor. From the equation, the Schmid factor is an effective indicator to describe the anisotropic yield behavior since it relates the yield strength to crystallographic orientation of grain. In this case, the yield anisotropic ratio R, i.e., the ratio of yield strength of A0 to A90 sample can be related to the Schmid factor as [66]:

$$R = \frac{\sigma_y^{A0}}{\sigma_y^{A90}} = \frac{\tau_s}{m^{A0}} \Big/ \frac{\tau_s}{m^{A90}} = \frac{m^{A90}}{m^{A0}}$$ (9)

where τ_s is the critical shear stress for a certain material and independent on loading direction. Fig. 10 shows the distribution of Schmid factor extracted from raw EBSD data. According to Eq. (9), the theoretical yield anisotropy ratio for μLPBFed and cLPBFed samples is 1.052 and 1.073, respectively, which agrees well with the experimental value 1.047 and 1.093 calculated through $\sigma_y^{A0}/\sigma_y^{A90}$. Therefore, the Schmid factor can provide valuable insight into the anisotropic yield strength caused

by the crystallographic texture in the LPBFed parts.
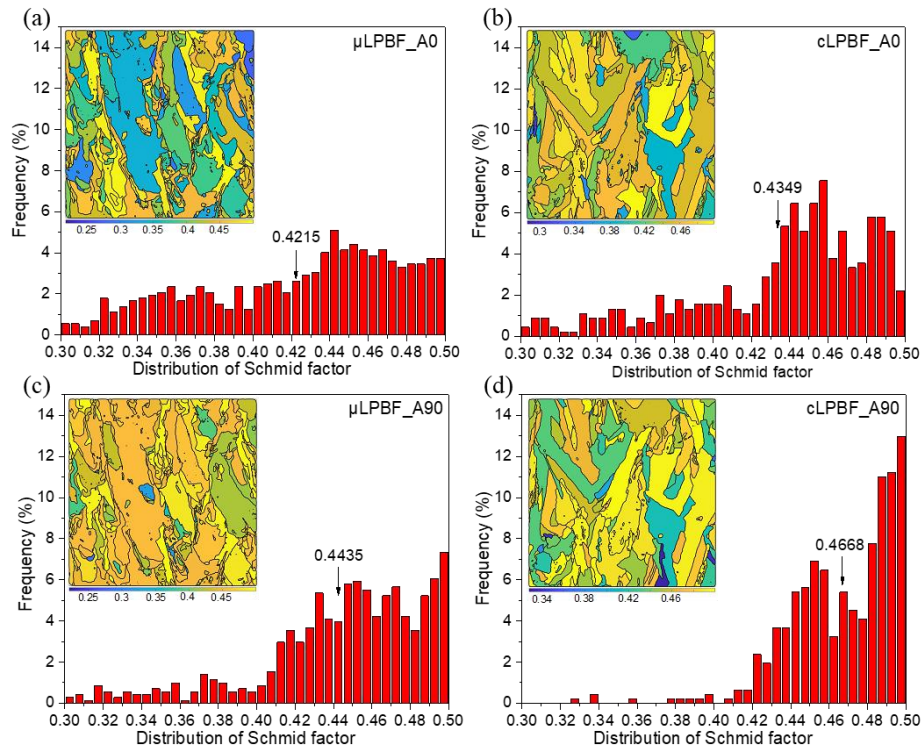
Fig. 10. Schmid factor distribution for: (a) μLPBF_A0, (b) μLPBF_A90, (c) cLPBF_0 and (D) cLPBF_90; the arrows denote the average value of Schmid factor.

b. Ductility and deformation behavior

Despite of the inherent pores after printing, both cLPBFed and μLPBFed samples exbibit a good ductility, which is comparable or even larger than that reported in [18]. It has been confirmed that the cellular structure plays an important role on the deformation behavior and the resultant good ductility. For austenitic SS316L, deformation occurs mainly by dislocation slip and mechanical twining. At a low strain, dislocation slip mechanism dominates during tensile deformation. The pinning effect of micro segregated elements leads to dislocation strapping along the cell walls. Thus, the interaction between dislocations and cell walls creates a progressive work-hardening behavior [18]. With increasing strain, deformation twining becomes increasingly important, which has been confirmed in [18]. Twining activity is considered as an important contributor to the high ductility of LPBFed materials, especially for vertically built (A90) samples [19]. Twining activity dynamically

refines the microstructure by introducing twining boundaries and interacting with the dislocation networks, which maintains a steady work-hardening ability and delays the onset of plastic instability.

Anisotropic ductility and deformation behavior are also observed in this work, where A90 sample shows a significantly higher elongation and a steadier work hardening behavior compared with A0 sample. Similar results for MAM built SS316L and other alloys have also been reported [19, 67]. The higher elongation along building direction is most likely attributed to the columnar grains and the vertically oriented grain boundaries, along which the damage can be preferentially tolerated, leading to a larger plastic deformation [67]. In addition, it is known that deformation twining activity is dependent on the initial crystallographic texture with respect to loading direction. Thus, the different deformation behaviors possibly indicate that different dominant deformation mechanisms might be activated along different loading directions.

4.3 Cantilever distortion

The cantilever deflection for cLPBF is about 40% higher than the average deformation for μLPBF, reflecting a greater macroscopic residual stress for cLPBF process. The differences of deformation between two types of LPBF processes are attributed to the molten pool size and the thermal histories. Commonly, a hatch angle of 67 ° between every layer could change the direction of stress shrinkage between every layer to avoid horizontal cumulative effect. As a result, the horizontal residual stresses parallel to the scanning directions cancel out most of each other layer by layer in the μLPBF. In spite of applying this approach, warping and crack still occurs during LPBF process. This is because vertical shrinkage is unavoidable. Due to the difference of laser spot size, a layer thickness of 0.03 mm to 0.05 mm is usually chosen in cLPBF, while μLPBF uses a layer thickness of 0.01 mm to match its molten pool size in order to melt metal powder properly. The cLPBF creates a larger molten

pool and an accompanying larger volume shrinkage of the molten pool after solidification. Under the high cooling rate and high-speed scanning, the melting and solidification processes are completed in a considerably short period of time. The shrinkage of top layers is restricted by the underlying layers due to the temperature gradient in the depth direction. As a result, the larger residual stress in the depth direction is expected in cLPBF due to the larger volume shrinkage. On the other hand, there are more thermal cycles in μLPBF for a given part due to its smaller laser track and layer thickness, and the residual stress can be partially relieved for a more significant in-situ stress relief annealing. Hence, it is the different molten pools and thermal cycles which result in the difference of residual stress and the resultant different deflections of the printed parts. As to the four groups of μLPBFed cantilevers, a lower scanning speed and a higher laser power lead to a larger energy input which results in a larger molten pool size and larger deflection [68]. Therefore, the part distortion can be controlled by adjusting the process parameters.

5. Conclusions

In this work, the μLPBF is comprehensively compared with the conventional LPBF in fabrication of SS316L components. The surface quality, crystallographic microstructure, solidification cellular structure, mechanical properties and distortion of the printed parts are studied, and the underlying mechanisms are discussed. The main conclusions are drawn as follows:

1) A better surface finish after μLPBF is obtained, with top and side surface roughness (Ra) measured as 3.40 and 5.66 μm. The larger laser beam and larger powder size are responsible for the poorer surface quality in cLPBF.

2) A stronger <110> texture is developed in μLPBFed sample. The average grain size is about 7.16 μm, smaller than that of cLPBF (10.31 μm). Both μLPBFed and cLPBFed samples have a higher fraction of LAGBs than HAGBs. A higher density of LAGBs and GNDs in μLPBF is detected than that in cLPBF.

3) cLPBF creates a cellular structure with the average cell size of 866.8 nm, which is over two times larger than the μLPBFed ones. Higher cell wall thickness of 128.6 nm is measured for the cLPBFed samples, suggesting a more significant compositional segregation. The overall difference in microstructure is caused by the different thermal cycling histories and molten pool conditions between cLPBF and μLPBF.

4) The yield strength of μLPBFed sample is marginally lower than cLPBFed one, while the ductility is comparable. It is concluded that the compositional microsegregation in the cellular structures is responsible for the strength difference between cLPBFed and μLPBFed samples. Future work is needed to differentiate the contribution of compositional microsegregation from dislocation cells.

5) The cantilever distortion for cLPBF is about 40% higher than the average distortion for μLPBF, reflecting a greater macroscopic residual stress of the cLPBF process. The different molten pools and thermal cycles are responsible for the difference of residual stress and the resultant different deflections of parts.

6) The microstructure, mechanical properties and part distortion of μLPBFed samples remain at the same level with the variation of laser power and scanning speed. Both cLPBFed and μLPBFed samples show anisotropy in terms of yield strength, ductility and deformation behavior.

References

[1] T. DebRoy, H.L. Wei, J.S. Zuback, T. Mukherjee, J.W. Elmer, J.O. Milewski, A.M.

Beese, A. Wilson-Heid, A. De, W. Zhang, Additive manufacturing of metallic components – Process, structure and properties, Prog. Mater. Sci. 92 (2018) 112-224.

[2] J.P. Oliveira, A.D. LaLonde, J. Ma, Processing parameters in laser powder bed fusion metal additive manufacturing, Mater. Des. 193 (2020) 108762.

[3] J.P. Oliveira, T.G. Santos, R.M. Miranda, Revisiting fundamental welding concepts to improve additive manufacturing: From theory to practice, Prog. Mater. Sci. 107 (2020) 100590.

[4] M.L. Montero-Sistiaga, M. Godino-Martinez, K. Boschmans, J.-P. Kruth, J. Van Humbeeck, K. Vanmeensel, Microstructure evolution of 316L produced by HP-SLM (high power selective laser melting), Addit. Manuf. 23 (2018) 402-410.

[5] F. Calignano, M. Lorusso, J. Pakkanen, F. Trevisan, E.P. Ambrosio, D. Manfredi, P. Fino, Investigation of accuracy and dimensional limits of part produced in aluminum alloy by selective laser melting, Int. J. Adv. Manuf. Tech. 88 (1-4) (2017) 451-458.

[6] H. Hassanin, F. Modica, M.A. El-Sayed, J. Liu, K. Essa, Manufacturing of Ti–6Al–4V Micro-Implantable Parts Using Hybrid Selective Laser Melting and Micro-Electrical Discharge Machining, Adv. Eng. Mater. 18(9) (2016) 1544-1549.

[7] L. Zhang, S. Feih, S. Daynes, S. Chang, M.Y. Wang, J. Wei, W.F. Lu, Energy absorption characteristics of metallic triply periodic minimal surface sheet structures under compressive loading, Addit. Manuf. 23 (2018) 505-515.

[8] M. Vaezi, H. Seitz, S.F. Yang, A review on 3D micro-additive manufacturing technologies, Int. J. Adv. Manuf. Tech. 67 (5-8) (2013) 1721-1754.

[9] B. Nagarajan, Z.H. Hu, X. Song, W. Zhai, J. Wei, Development of Micro Selective Laser Melting: The State of the Art and Future Perspectives, Engineering 5(4) (2019) 702-720.

[10] J. Fu, Z.H. Hu, X. Song, W. Zhai, Y. Long, H. Li, M.W. Fu, Micro selective laser melting of NiTi shape memory alloy: Defects, microstructures and thermal/mechanical properties, Opt. Laser Technol. 131 (2020) 106374.

[11] Z.H. Hu, B. Nagarajan, X. Song, R. Huang, W. Zhai, J. Wei, Formation of SS316L Single Tracks in Micro Selective Laser Melting: Surface, Geometry, and

Defects, Adv. Mater. Sci. Eng. 2019 (2019) 9451406.

[12] C.Y. Yap, C.K. Chua, Z.L. Dong, Z.H. Liu, D.Q. Zhang, L.E. Loh, S.L. Sing, Review of selective laser melting: Materials and applications, Appl. Phys. Rev. 2(4) (2015) 041101.

[13] J.L. Zhang, B. Song, Q.S. Wei, D. Bourell, Y.S. Shi, A review of selective laser melting of aluminum alloys: Processing, microstructure, property and developing trends, J. Mater. Sci. Technol. 35(2) (2019) 270-284.

[14] L.C. Zhang, H. Attar, Selective laser melting of titanium alloys and titanium matrix composites for biomedical applications: a review, Adv. Eng. Mater. 18(4) (2016) 463-475.

[15] E.O. Olakanmi, R. Cochrane, K. Dalgarno, A review on selective laser sintering/melting (SLS/SLM) of aluminium alloy powders: Processing, microstructure, and properties, Prog. Mater. Sci. 74 (2015) 401-477.

[16] B. Song, S.J. Dong, B.C. Zhang, H.L. Liao, C. Coddet, Effects of processing parameters on microstructure and mechanical property of selective laser melted Ti6Al4V, Mater. Des. 35 (2012) 120-125.

[17] J. Dilip, G.J. Ram, T.L. Starr, B. Stucker, Selective laser melting of HY100 steel: process parameters, microstructure and mechanical properties, Addit. Manuf. 13 (2017) 49-60.

[18] Y.M. Wang, T. Voisin, J.T. McKeown, J. Ye, N.P. Calta, Z. Li, Z. Zeng, Y. Zhang, W. Chen, T.T. Roehling, R.T. Ott, M.K. Santala, P.J. Depond, M.J. Matthews, A.V. Hamza, T. Zhu, Additively manufactured hierarchical stainless steels with high strength and ductility, Nat. Mater. 17(1) (2018) 63-71.

[19] M. Shamsujjoha, S.R. Agnew, J.M. Fitz-Gerald, W.R. Moore, T.A. Newman, High Strength and Ductility of Additively Manufactured 316L Stainless Steel Explained, Metall. Mater. Trans. A 49 (2018) 3011-3027.

[20] D. Kong, C. Dong, S. Wei, X. Ni, L. Zhang, R. Li, L. Wang, C. Man, X. Li, About metastable cellular structure in additively manufactured austenitic stainless steels, Addit. Manuf. 38 (2021) 101804.

[21] T. Niendorf, S. Leuders, A. Riemer, H.A. Richard, T. Tröster, D. Schwarze, Highly anisotropic steel processed by selective laser melting, Metall. Mater. Trans. B 44(4) (2013) 794-796.

[22] Z.J. Sun, X.P. Tan, S.B. Tor, C.K. Chua, Simultaneously enhanced strength and ductility for 3D-printed stainless steel 316L by selective laser melting, NPG Asia Mater. 10(4) (2018) 127-136.

[23] D. Wang, Y. Liu, Y.Q. Yang, D.M. Xiao, Theoretical and experimental study on surface roughness of 316L stainless steel metal parts obtained through selective laser melting, Rapid Prototyp. J. 22(4) (2016) 706-716.

[24] M. Yakout, M.A. Elbestawi, S.C. Veldhuis, Density and mechanical properties in selective laser melting of Invar 36 and stainless steel 316L, J. Mater. Process. Technol. 266 (2019) 397-420.

[25] A. Rottger, J. Boes, W. Theisen, M. Thiele, C. Esen, A. Edelmann, R. Hellmann, Microstructure and mechanical properties of 316L austenitic stainless steel processed by different SLM devices, Int. J. Adv. Manuf. Tech. 108(3) (2020) 769-783.

[26] J. Metelkova, Y. Kinds, K. Kempen, C. de Formanoir, A. Witvrouw, B. Van Hooreweder, On the influence of laser defocusing in Selective Laser Melting of 316L, Addit. Manuf. 23 (2018) 161-169.

[27] F. Bachmann, R. Hielscher, H. Schaeben, Grain detection from 2d and 3d EBSD data—Specification of the MTEX algorithm, Ultramicroscopy 111(12) (2011) 1720-1733.

[28] W. Pantleon, Resolving the geometrically necessary dislocation content by conventional electron backscattering diffraction, Script. Mater. 58(11) (2008) 994-997.

[29] L. Cui, S. Jiang, J. Xu, R.L. Peng, R.T. Mousavian, J. Moverare, Revealing relationships between microstructure and hardening nature of additively manufactured 316L stainless steel, Mater. Des. 198 (2020) 109385.

[30] C.Y. Zhu, T. Harrington, G.T. Gray, K.S. Vecchio, Dislocation-type evolution in quasi-statically compressed polycrystalline nickel, Acta Mater. 155 (2018) 104-116.

[31] O. Muransky, L. Balogh, M. Tran, C. Hamelin, J.-S. Park, M.R. Daymond, On the measurement of dislocations and dislocation substructures using EBSD and HRSD techniques, Acta Mater. 175 (2019) 297-313.

[32] H. Zhi, C. Zhang, S. Antonov, H. Yu, T. Guo, Y. Su, Investigations of dislocation-type evolution and strain hardening during mechanical twinning in Fe-22Mn-0.6 C twinning-induced plasticity steel, Acta Mater. 195 (2020) 371-382.

[33] G. Strano, L. Hao, R.M. Everson, K.E. Evans, Surface roughness analysis, modelling and prediction in selective laser melting, J. Mater. Process. Technol. 213(4) (2013) 589-597.

[34] Y.J. Yin, J.Q. Sun, J. Guo, X.F. Kan, D.C. Yang, Mechanism of high yield strength and yield ratio of 316 L stainless steel by additive manufacturing, Mater. Sci. Eng., A 744 (2019) 773-777.

[35] S. Gao, Z. Hu, M. Duchamp, P.S.S.R. Krishnan, S. Tekumalla, X. Song, M. Seita, Recrystallization-based grain boundary engineering of 316L stainless steel produced via selective laser melting, Acta Mater. 200 (2020) 366-377.

[36] O. Andreau, I. Koutiri, P. Peyre, J.-D. Penot, N. Saintier, E. Pessard, T. De Terris, C. Dupuy, T. Baudin, Texture control of 316L parts by modulation of the melt pool morphology in selective laser melting, J. Mater. Process. Technol. 264 (2019) 21-31.

[37] A.J. Wilkinson, D. Randman, Determination of elastic strain fields and geometrically necessary dislocation distributions near nanoindents using electron back scatter diffraction, Philos. Mag. 90(9) (2010) 1159-1177.

[38] T. Voisin, J.-B. Forien, A. Perron, S. Aubry, N. Bertin, A. Samanta, A. Baker, Y.M. Wang, New insights on cellular structures strengthening mechanisms and thermal stability of an austenitic stainless steel fabricated by laser powder-bed-fusion, Acta Mater. 203 (2021) 116476.

[39] F. Yan, W. Xiong, E. Faierson, G.B. Olson, Characterization of nano-scale oxides in austenitic stainless steel processed by powder bed fusion, Script. Mater. 155 (2018) 104-108.

[40] J.H. Hollomon, Tensile deformation, Aime Trans 12(4) (1945) 1-22.

[41] A.M. Rausch, M. Markl, C. Korner, Predictive simulation of process windows for powder bed fusion additive manufacturing: Influence of the powder size distribution, Comput. Math. with Appl. 78(7) (2019) 2351-2359.

[42] A.B. Spierings, N. Herres, G. Levy, Influence of the particle size distribution on surface quality and mechanical properties in AM steel parts, Rapid Prototyp. J. (2011).

[43] R. Li, J. Liu, Y. Shi, L. Wang, W. Jiang, Balling behavior of stainless steel and nickel powder during selective laser melting process, Int. J. Adv. Manuf. Technol. 59(9-12) (2012) 1025-1035.

[44] K. Mumtaz, N. Hopkinson, Top surface and side roughness of Inconel 625 parts processed using selective laser melting, Rapid Prototyp. J. 15(2) (2009) 96-103.

[45] S. Dryepondt, P. Nandwana, P. Fernandez-Zelaia, F. List, Microstructure and high temperature tensile properties of 316L fabricated by laser powder-bed fusion, Addit. Manuf. 37 (2021) 101723.

[46] M.-S. Pham, B. Dovgyy, P.A. Hooper, C.M. Gourlay, A. Piglione, The role of side-branching in microstructure development in laser powder-bed fusion, Nat. Commun. 11(1) (2020) 749.

[47] N. Nadammal, T. Mishurova, T. Fritsch, I. Serrano-Munoz, A. Kromm, C. Haberland, P.D. Portella, G. Bruno, Critical role of scan strategies on the development of microstructure, texture, and residual stresses during laser powder bed fusion additive manufacturing, Addit. Manuf. 38 (2021) 101792.

[48] H.Y. Wan, Z.J. Zhou, C.P. Li, G.F. Chen, G.P. Zhang, Effect of scanning strategy on grain structure and crystallographic texture of Inconel 718 processed by selective laser melting, J. Mater. Sci. Technol. 34(10) (2018) 1799-1804.

[49] K.G. Prashanth, J. Eckert, Formation of metastable cellular microstructures in selective laser melted alloys, J. Alloys Compd. 707 (2017) 27-34.

[50] J.W. Elmer, S.M. Allen, T.W. Eagar, Microstructural Development during Solidification of Stainless-Steel Alloys, Metall. Trans. A 20(10) (1989) 2117-2131.

[51] K.M. Bertsch, G. Meric de Bellefon, B. Kuehl, D.J. Thoma, Origin of dislocation

structures in an additively manufactured austenitic stainless steel 316L, Acta Mater. 199 (2020) 19-33.

[52] Y. Wang, C. Zhang, C. Yu, L. Xing, K. Li, J. Chen, J. Ma, W. Liu, Z. Shen, Construction of Cellular Substructure in Laser Powder Bed Fusion, Metals 9(11) (2019) 1231.

[53] H. Choo, K.L. Sham, J. Bohling, A. Ngo, X.H. Xiao, Y. Ren, P.J. Depond, M.J. Matthews, E. Garlea, Effect of laser power on defect, texture, and microstructure of a laser powder bed fusion processed 316L stainless steel, Mater. Des. 164 (2019) 107534.

[54] K. Saeidi, X. Gao, Y. Zhong, Z.J. Shen, Hardened austenite steel with columnar sub-grain structure formed by laser melting, Mater. Sci. Eng., A 625 (2015) 221-229.

[55] B. Barkia, P. Aubry, P. Haghi-Ashtiani, T. Auger, L. Gosmain, F. Schuster, H. Maskrot, On the origin of the high tensile strength and ductility of additively manufactured 316L stainless steel: Multiscale investigation, J. Mater. Sci. Technol. 41 (2020) 209-218.

[56] A.J. Birnbaum, J.C. Steuben, E.J. Barrick, A.P. Iliopoulos, J.G. Michopoulos, Intrinsic strain aging, $\Sigma 3$ boundaries, and origins of cellular substructure in additively manufactured 316L, Addit. Manuf. 29 (2019) 100784.

[57] L. Liu, Q. Ding, Y. Zhong, J. Zou, J. Wu, Y.-L. Chiu, J. Li, Z. Zhang, Q. Yu, Z. Shen, Dislocation network in additive manufactured steel breaks strength–ductility trade-off, Mater. Today 21(4) (2018) 354-361.

[58] P. Krakhmalev, G. Fredriksson, K. Svensson, I. Yadroitsev, I. Yadroitsava, M. Thuvander, R. Peng, Microstructure, Solidification Texture, and Thermal Stability of 316 L Stainless Steel Manufactured by Laser Powder Bed Fusion, Metals 8(8) (2018) 643.

[59] R. Napolitano, R. Schaefer, The convergence-fault mechanism for low-angle boundary formation in single-crystal castings, J. Mater. Sci. 35(7) (2000) 1641-1659.

[60] K. Ma, H. Wen, T. Hu, T.D. Topping, D. Isheim, D.N. Seidman, E.J. Lavernia, J.M. Schoenung, Mechanical behavior and strengthening mechanisms in ultrafine

grain precipitation-strengthened aluminum alloy, Acta Mater. 62 (2014) 141-155.

[61] S.V. Astafurov, G.G. Maier, E.V. Melnikov, V.A. Moskvina, M.Y. Panchenko, E.G. Astafurova, The strain-rate dependence of the Hall-Petch effect in two austenitic stainless steels with different stacking fault energies, Mater. Sci. Eng., A 756 (2019) 365-372.

[62] T.R. Smith, J.D. Sugar, C. San Marchi, J.M. Schoenung, Strengthening mechanisms in directed energy deposited austenitic stainless steel, Acta Mater. 164 (2019) 728-740.

[63] Y. Kok, X.P. Tan, P. Wang, M.L.S. Nai, N.H. Loh, E. Liu, S.B. Tor, Anisotropy and heterogeneity of microstructure and mechanical properties in metal additive manufacturing: A critical review, Mater. Des. 139 (2018) 565-586.

[64] A. Charmi, R. Falkenberg, L. Avila, G. Mohr, K. Sommer, A. Ulbricht, M. Sprengel, R.S. Neumann, B. Skrotzki, A. Evans, Mechanical anisotropy of additively manufactured stainless steel 316L: An experimental and numerical study, Mater. Sci. Eng., A 799 (2021) 140154.

[65] D. Gu, H. Chen, Selective laser melting of high strength and toughness stainless steel parts: The roles of laser hatch style and part placement strategy, Mater. Sci. Eng., A 725 (2018) 419-427.

[66] Z. Lei, P. Gao, X. Wang, M. Zhan, H. Li, Analysis of anisotropy mechanism in the mechanical property of titanium alloy tube formed through hot flow forming, J. Mater. Sci. Technol. 86 (2021) 77-90.

[67] B.E. Carroll, T.A. Palmer, A.M. Beese, Anisotropic tensile behavior of Ti–6Al–4V components fabricated with directed energy deposition additive manufacturing, Acta Mater. 87 (2015) 309-320.

[68] Y. Liu, Y. Yang, D. Wang, A study on the residual stress during selective laser melting (SLM) of metallic powder, Int. J. Adv. Manuf. Technol. 87(1-4) (2016) 647-656.